Impacts of Updraft Size and Dimensionality on the Perturbation Pressure and Vertical Velocity in Cumulus Convection. Part I: Simple, Generalized Analytic Solutions

HUGH MORRISON

National Center for Atmospheric Research, Boulder, Colorado*

(Manuscript received 28 January 2015, in final form 17 July 2015)

ABSTRACT

This study investigates relationships between vertical velocity, perturbation pressure, updraft size, and dimensionality for cumulus convection. Generalized theoretical expressions are derived from approximate analytic solutions of the governing momentum and mass continuity equations for both two-dimensional (2D) and axisymmetric quasi-three-dimensional (3D) steady-state updrafts. These expressions relate perturbation pressure and vertical velocity to updraft radius R, height H, and thermal buoyancy. They suggest that the vertical velocity at the level of neutral buoyancy is reduced from perturbation pressure effects by factors of $\sqrt{1+8L_c^2}$ and $\sqrt{1+2L_c^2}$ in 2D and 3D, respectively, where $L_c \equiv \alpha R/H$ is a nondimensional length, with somewhat different scalings lower in the updraft (α is a parameter equal to the ratio of vertical velocity horizontally averaged across the updraft to that at the updraft center). They also indicate that updrafts are weaker in 2D than 3D, all else being equal, with a difference of up to a factor of 2 in vertical velocity for $L_c \gg 1$ as a direct result of differences in mass continuity between 2D and axisymmetric 3D flow. Differences between these expressions and other analytic solutions, including those derived from single normal mode Fourier/Fourier–Bessel expansion of the buoyant perturbation pressure Poisson equation, are discussed. Part II of this study compares the theoretical expressions with numerical solutions of the buoyant perturbation pressure Poisson equation for a wide range of thermal buoyancy profiles representing shallow-to-deep moist convection and also with fully dynamical 2D and 3D updraft simulations.

1. Introduction

The importance of perturbation pressure on cumulus convection has been long established. Early observations at the surface from direct pressure measurements indicated perturbations on the order of 1 hPa for airmass thunderstorms (Byers and Braham 1949; Fujita 1955). Later in-cloud measurements showed hydrostatic pressure perturbations of 3 hPa at a height of 6 km and a pressure deficit of 1 hPa near cloud base (Barnes 1970). Several modeling studies (e.g., Árnason et al. 1968; Soong and Ogura 1973; Schlesinger 1973; Wilhelmson 1974; Yau 1979; Kuo and Raymond 1980; Schlesinger 1984; Parker 2010) have shown that mid- and upper-level thermal buoyancy[1] is partly opposed by a downward-directed vertical perturbation pressure gradient force in convective updrafts [e.g., see the review of Doswell and Markowski (2004)]. In environments with strong vertical shear of the horizontal wind, dynamic perturbation pressure can also lead to an upward-directed perturbation pressure gradient force and enhanced vertical motion, as well as cell splitting (i.e., supercells) (Rotunno and Klemp 1982; Klemp 1987).

For upright and nonrotating updrafts, it is well known that the degree to which the buoyancy is offset by the

* The National Center for Atmospheric Research is sponsored by the National Science Foundation.

Corresponding author address: Hugh Morrison, National Center for Atmospheric Research, 3090 Center Green Drive, Boulder, CO 80301.
E-mail: morrison@ucar.edu

DOI: 10.1175/JAS-D-15-0040.1

[1] Thermal buoyancy is the perturbation buoyancy relative to a horizontally homogeneous, typically hydrostatic background state. While thermal buoyancy depends on the particular background state chosen, the combination of thermal buoyancy and buoyant perturbation pressure, relevant for vertical acceleration, is independent of the mean state [for further discussion, see Davies-Jones (2003) and Doswell and Markowski (2004)]. Herein, "buoyancy" will refer to thermal or Archimedean buoyancy.

perturbation pressure gradient force depends in part on the updraft width (i.e., the width of the buoyant region) and, more specifically, on the ratio of updraft width and height. Physically, this is explained by the need for higher perturbation pressure in the upper part of the updraft to push more air laterally away and lower pressure in the lower part to draw more air into its wake, for wide compared to narrow updrafts (Markowski and Richardson 2010; Trapp 2013; Bluestein 2013). Using a time-dependent axisymmetric plume model, Holton (1973) showed that perturbation pressure gradient forces can significantly reduce the cloud growth rate as the updraft width increases. Kuo and Raymond (1980) showed a strong dependence of perturbation pressure effects and, hence, vertical velocity on updraft width for both shallow and deep convection, using a steady-state axisymmetric plume model.

Weisman et al. (1997) used normal mode solutions to the linearized, two-dimensional (2D) Boussinesq equations of motion, continuity, and thermodynamics to derive a simple scaling of w with updraft width and height [(4) in Weisman et al. 1997]:

$$W_0 \approx \frac{k}{\sqrt{k^2 + l^2}} \frac{B_0}{N}, \tag{1}$$

where W_0 and B_0 are the amplitudes of the normal modes corresponding to the vertical velocity and buoyancy, respectively; N is the Brunt–Väisälä frequency; and k and l are the horizontal and vertical wavenumbers, respectively (all symbols used in the paper are defined in Table 1). Using $k = 2\pi/K$ and $l = 2\pi/L$ (where K and L are the horizontal and vertical scales of the buoyancy perturbation), (1) can be expressed as

$$W_0 \approx \frac{1}{\sqrt{1 + K^2/L^2}} \frac{B_0}{N}. \tag{2}$$

Thus, there is a dependence of vertical velocity on a thermodynamic parameter B_0/N and a dimensionless length parameter $1/\sqrt{1 + K^2/L^2}$, which reduces to a dependence on L/K for the hydrostatic regime ($K^2/L^2 \gg 1$). Weisman et al. (1997) used the vorticity form of the 2D governing equations to derive this scaling and hence did not explicitly relate (1) to perturbation pressure. Nonetheless, this forms the basis for a qualitative understanding of the effects of K and L on updraft strength, especially in the limits as $K/L \to 0$ or $K/L \to \infty$.

Several studies have also shown that, for a given buoyant forcing, 2D updrafts are weaker than their three-dimensional (3D) counterparts (e.g., Wilhelmson 1974; Schlesinger 1984; Lipps and Hemler 1986; Tao et al. 1987; Redelsperger et al. 2000; Phillips and Donner 2006; Zeng et al. 2008). Zeng et al. (2008) used forced mode solutions to the linearized 2D and 3D equations of motion and showed weaker vertical velocity in 2D than 3D for a given mode. Murray (1970) attributed the weakness of 2D updrafts to inherent differences in convergence, with horizontally averaged convergence a factor of 2 larger in 3D than 2D. Perturbation pressure has also been invoked to explain these differences, with a greater compensation of the thermal buoyancy by the downward-directed perturbaion pressure force in 2D compared to 3D (Soong and Ogura 1973; Yau 1979; Schlesinger 1984). Schlesinger (1984) stated that the perturbation pressure explanation provides a more ''physically compelling argument'' for differences in updraft strength in 2D and 3D than convergence. Herein, it is shown that differences in the downward-directed perturbation pressure gradient force are intrinsically linked to differences in convergence between 2D and 3D, providing a bridge between these explanations.

The overall goal of this study is to gain insight and quantitative understanding of the physical mechanisms governing perturbation pressure effects on cumulus convection, especially with regard to updraft size and dimensionality (2D vs 3D). While the importance of updraft size and dimensionality on cumulus dynamics via perturbation pressure effects has been long known, a deeper, more quantitative understanding remains limited. To address this issue, theoretical expressions relating perturbation pressure, vertical velocity, updraft width and height, and convective available potential energy (CAPE) are derived based on approximate analytic solutions to the governing momentum and mass continuity equations. These expressions are simple and have a clear physical meaning and interpretation.

Morrison (2015, hereafter Part II) compares the analytic theoretical expressions with numerical solutions of the buoyant perturbation pressure Poisson equation for various buoyancy profiles representing shallow-to-deep moist convection over a range of updraft radii and for 2D and 3D. The theoretical expressions are also compared to fully dynamical 2D and 3D updraft simulations initiated with warm bubbles of various sizes. Part II discusses these results in the context of biases in ''gray zone'' models with a horizontal grid spacing Δx of $O(1–10)$ km, given that updraft width at these resolutions approximately scales with Δx, and proposes simple expressions for improving the treatment of perturbation pressure in convection parameterizations.

The remainder of this paper is organized as follows. Section 2 presents an overview of single normal mode solutions to the buoyant perturbation pressure Poisson equation in 2D and 3D. Section 3 presents a derivation of the generalized theoretical expressions. Discussion is

TABLE 1. List of symbols.

B_0	Amplitude of the single normal mode thermal buoyancy
c_0	Constant associated with the single normal mode Fourier–Bessel expansion, $c_0 \approx \pi^2/(2 \times 2.41^2) \approx 0.849$
CAPE	Vertical integral of thermal buoyancy from the LFC to LNB
CAPE_1	Vertical integral of thermal buoyancy from the LFC to LMB
CAPE_2	Vertical integral of thermal buoyancy from the LMB to LNB
D	Updraft diameter
g	Acceleration of gravity
H	Updraft height, defined as the difference in height from the LNB to LFC
H_1	Distance from the LMB to LFC
H_2	Distance from the LNB to LMB
J_0	Bessel function of the first kind
K	Horizontal wavelength
k	Horizontal wavenumber
k_B	First root of the Bessel function of the first kind
L	Vertical wavelength
l	Vertical wavenumber
L_c	Nondimensional length parameter related to updraft aspect ratio
N	Brunt–Väisälä frequency
p	Perturbation pressure
p_B	Buoyant perturbation pressure
p_D	Dynamic perturbation pressure
p_H	Hydrostatic perturbation pressure
p_F	Perturbation pressure at the LFC
p_M	Perturbation pressure at the LMB
p_N	Perturbation pressure at the LNB
p_{NH}	Nonhydrostatic perturbation pressure
p_R	Perturbation pressure at updraft lateral edge
R	Updraft radius
r	Radial distance
t	Time
u	Horizontal air velocity
$\mathbf{v}$	Wind vector
u_R	Horizontal wind velocity at the updraft lateral edge
w	Vertical air velocity
W_0	Amplitude of the normal mode vertical velocity
w_0	Vertical air velocity at the updraft center
w_F	Vertical air velocity at the LFC
w_M	Vertical air velocity at the LMB
w_N	Vertical air velocity at the LNB
x	Horizontal distance
z	Height
z_F	Height of the LFC
z_M	Height of the LMB
z_N	Height of the LNB
α	Parameter equal to the ratio of w averaged horizontally across the updraft to that at the updraft center
Δp	Perturbation pressure difference between the LNB and LFC
Δp_1	Perturbation pressure difference between the LMB and LFC
Δp_2	Perturbation pressure difference between the LNB and LMB
ρ	Air density
ρ_0	Boussinesq air density

provided in section 4, and a summary and conclusions are given in section 5.

2. Single normal mode solutions

A diagnostic equation for perturbation pressure can be obtained by multiplying the inviscid, anelastic momentum equation (Ogura and Phillips 1962) by background air density $\overline{\rho}$, taking its divergence, and rearranging terms to yield (e.g., Klemp 1987; Markowski and Richardson 2010)

$$\nabla^2 p = \nabla^2 p_D + \nabla^2 p_B = -\nabla \cdot (\overline{\rho}\mathbf{v} \cdot \nabla \mathbf{v}) + \frac{\partial(\overline{\rho} B)}{\partial z}, \qquad (3)$$

where $\mathbf{v}$ is the wind vector (u and w are the horizontal and vertical components in 2D, respectively), p is the air pressure, and $B = -[\rho/\overline{\rho}(z)]g$ is the buoyancy (g is the

gravitational acceleration). Coriolis acceleration is neglected. All quantities represent perturbations from a hydrostatic, motionless, horizontally homogeneous background state, except for the height-varying background density $\overline{\rho}(z)$. Hereinafter, the overbar representing the background density is omitted. In (3), the terms associated with perturbation pressure are separated into a dynamic component p_D, associated with the first term on the right-hand side of (3), and a buoyant component p_B, associated with the second term on the right-hand side, as is often done. The perturbation pressure can also be separated into hydrostatic and nonhydrostatic components so that $p = p_H + p_{\rm NH}$. The hydrostatic part p_H is given by the hydrostatic equation $\partial p_H/\partial z = \rho B$. The nonhydrostatic part $p_{\rm NH}$ is responsible for vertical acceleration such that $\partial p_{\rm NH}/\partial z = -\rho Dw/Dt$.

The wind field and various components of perturbation pressure (p_H, $p_{\rm NH}$, p_B, and p_D) are illustrated in Fig. 1 for an idealized, growing convective updraft simulated using the nonhydrostatic, compressible Cloud Model 1 (CM1; Bryan and Fritsch 2002), similar to Fig. 2.7 in Markowski and Richardson (2010). The simulation is 3D and uses 200-m horizontal and vertical grid spacings over a domain of $60 \times 60 \times 20\,\text{km}^3$. The updraft is initiated using a warm bubble with a maximum perturbation potential temperature of 2 K, a horizontal radius of 3 km, a vertical radius of 1.5 km, centered at an altitude of 1.5 km, and with perturbation potential temperature decreasing as a cosine function from the thermal center to its edge. Initial environmental thermodynamic conditions follow from the analytic sounding of Weisman and Klemp (1982), and the domain is initially motionless. Various components of perturbation pressure are calculated following the approach described in Markowski and Richardson (2010).

In weakly sheared environments such as in the simulation shown in Fig. 1, dynamic pressure perturbations lead to negative p along the updraft lateral edge associated with a vortex ring near the level of maximum buoyancy (LMB) (see Figs. 1d,h). However, the magnitude of $\partial p_D/\partial z$ tends to be much smaller than that of $\partial p_B/\partial z$ in most of the updraft core (Figs. 1g,h). This is explained by the fact that, in a horizontally symmetric updraft with $u = 0$ at the updraft center, the rotational contribution to $\nabla^2 p_D$, given by the term $(\partial w/\partial x)(\partial u/\partial z)$, is zero, although there is still a contribution to $\nabla^2 p_D$ from $(\partial u/\partial x)^2$ and $(\partial w/\partial z)^2$ at the updraft center (this is for 2D; a similar argument can be made for 3D). Additional simulations (not shown) with updrafts of varying R/H, where R is the updraft radius and H is height, indicate that $\partial p_D/\partial z$ in the updraft center becomes relatively more important for narrow updrafts, because $|\partial p_B/\partial z|$ becomes smaller with decreasing R/H, while $|\partial p_D/\partial z|$ does not depend strongly on R/H. The latter is explained approximately by the fact that $(\partial w/\partial z)^2$ increases while $(\partial u/\partial x)^2$ decreases as R/H is reduced. The general structure of p_D in the core of narrow updrafts has maxima near the level of neutral buoyancy (LNB) and level of free convection (LFC), associated with maximum $(\partial w/\partial z)^2$ and $(\partial u/\partial x)^2$, and a minimum at midlevels near the LMB. (Note that here and throughout the paper, LNB refers to the maximum height of positive buoyancy realized within the updraft, which may not necessarily be equal to the level of neutral buoyancy calculated from a sounding, assuming adiabatic parcel ascent.) This has the effect of reducing $\partial p/\partial z$ in the lower part of the updraft but increasing it in the upper part. However, the magnitude of $\partial p_D/\partial z$ averaged between the LFC and LNB is small for narrow updrafts, and hence it has a limited impact on the average $\partial w/\partial z$ from the LFC to the LNB in the updraft core. The average $\partial p_D/\partial z$ is larger in the core of wider updrafts, associated with convergence near and below the LFC, but, as explained above, these vertical gradients of p_D tend to be much smaller than those of p_B.

Based on these results, it is reasonable to assume that $\nabla^2 p_D \approx 0$ in updraft cores in weakly sheared environments, and (3) reduces to

$$\nabla^2 p \approx \nabla^2 p_B = \frac{\partial(\rho B)}{\partial z}. \tag{4}$$

Numerical calculations in Part II directly solve (4) provided a field of ρB and appropriate boundary conditions, while the normal mode approach discussed below provides approximate solutions to (4).

If ρB is a simple periodic wavelike function, then analytic solutions to (4) can be readily derived. For 2D, the simplest such representation with the condition that ρB is zero along the lower, upper, and lateral updraft boundaries, thereby defining the updraft as a contiguous region of radius R and height H with $B > 0$, is the single normal mode (Bluestein 2013):

$$\rho B = \rho_0 B_0 \cos\left(\frac{\pi x}{2R}\right) \sin\left(\frac{\pi z}{H}\right), \tag{5}$$

where B_0 is the value of B at the updraft center (amplitude of the normal mode), and x and z are distances along the horizontal and vertical axes. For simplicity, a constant air density ρ_0 is assumed following the Boussinesq approximation. Here, the values of buoyancy are defined such that the average over a period is zero. This choice is arbitrary, however, and does not affect gradients of perturbation pressure relevant to the dynamics. Taking the vertical derivative of (5) and combining with (4), the resulting equation has a solution with $p = 0$ at the updraft center along the vertical axis ($z = H/2$) and along the lateral boundaries ($x = \pm R$), similar to Bluestein (2013):

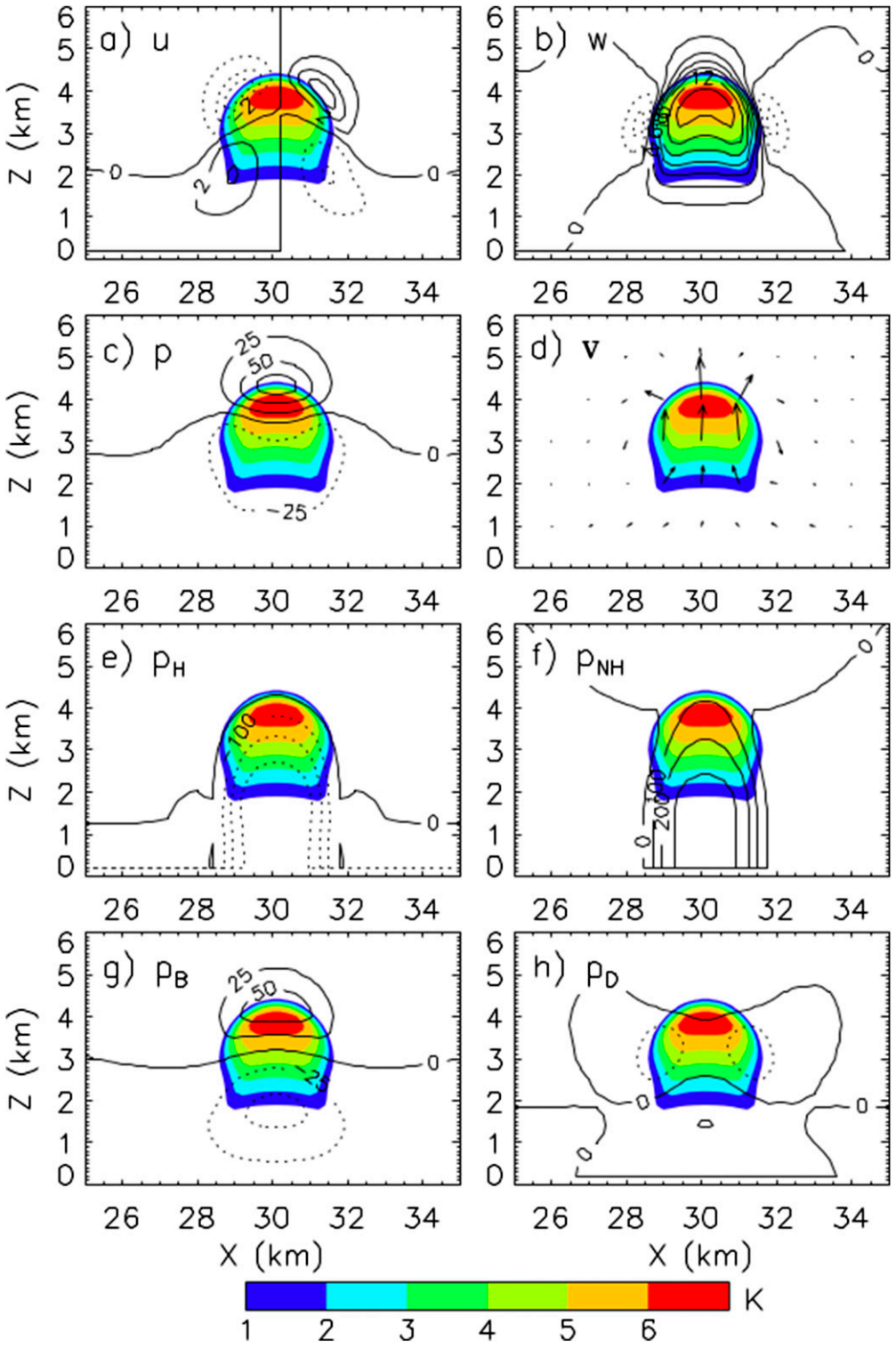

FIG. 1. Vertical cross section at the updraft center from a fully dynamical 3D simulation of an isolated convective updraft at 460 s, similar to Fig. 2.7 in Markowski and Richardson (2010): (a) horizontal wind u, (b) vertical wind w, (c) total perturbation pressure p, (d) 2D wind vector $\mathbf{v}$, (e) hydrostatic perturbation pressure p_H, (f) nonhydrostatic perturbation pressure p_{NH}, (g) buoyant perturbation pressure p_B, and (h) dynamic perturbation pressure p_D. Color contours show the perturbation potential temperature (relative to the initial environment) in all plots. The contour interval is 2 m s^{-1} for u and w; 25 hPa for p, p_B, and p_D; and 100 hPa for p_H and p_{NH}. Note that only part of the domain is shown.

$$p_B = -\frac{\rho_0 B_0}{\pi H}\left(\frac{1}{4R^2}+\frac{1}{H^2}\right)^{-1}\cos\left(\frac{\pi x}{2R}\right)\cos\left(\frac{\pi z}{H}\right). \quad (6)$$

The difference in p_B from the LNB to LFC at the updraft center Δp is found by evaluating (6) at $x = 0$ and $z = H$ and subtracting (6) evaluated at $x = 0$ and $z = 0$. This can be expressed in terms of $\text{CAPE} = \int_{\text{LFC}}^{\text{LNB}} B\,dz$ by integrating (5) from $z = 0$ to H, combining with the Δp evaluated from (6), and rearranging terms to yield

$$\Delta p = \rho_0 \text{CAPE}\left(1+\frac{H^2}{4R^2}\right)^{-1} \quad (7)$$

Note that, for consistency, CAPE is that relative to the horizontally averaged buoyancy of zero (over a period).

A similar expression for Δp can be derived for axisymmetric cylindrical quasi-3D updrafts using a Fourier–Bessel expansion. In this case, the single normal mode horizontal r component of the Laplacian in cylindrical coordinates is approximated as $-k_B^2 p$, where k_B is the first root of the Bessel function of the first kind, $J_0(k_B R) = 0$ (Holton 1973). This gives $k_B \sim 2.41/R$. Given that $J_0(0) = 1$, we can repeat the steps above to derive an expression for Δp in 3D analogous to (7):

$$\Delta p = \rho_0 \text{CAPE}\left(1+\frac{H^2}{2c_0 R^2}\right)^{-1}, \quad (8)$$

where $c_0 \approx \pi^2/(2\times 2.41^2) \approx 0.849$.

Equation (8) can be combined with the vertical momentum equation integrated from the LFC to the LNB at the updraft center, assuming a steady state, to yield an expression for w at the LNB, which is the maximum in the absence of entrainment. With the condition that $w = 0$ at the LFC, and assuming Boussinesq flow so that $\rho = \rho_0$, this yields

$$w_{\max} = \sqrt{2\text{CAPE}\left(1+\frac{2c_0 R^2}{H^2}\right)^{-1}} \quad (9)$$

for axisymmetric quasi-3D updrafts. A similar equation can be derived for 2D.

For less idealized forcing, equivalent solutions to (7)–(9) can be derived using a Fourier or Fourier–Bessel transform of ρB and retaining only the first term. However, some issues arise. First, the CAPE in (7)–(9) is that derived from vertical integration of the single normal mode representation of buoyancy from 0 to H. In general, this will be different from the actual CAPE unless the vertical integral of the single mode representation is exact. This can lead to large errors in the calculation of integrated quantities, such as Δp and w, and inconsistent behavior in the limits $R/H \to 0$ and $R/H \to \infty$. This problem can be circumvented by using the actual CAPE in (7)–(9), with the assumption that these scalings still apply, but the validity of such an approach is unclear. Second, expansion using Fourier or Fourier–Bessel series is valid only for periodic forcing functions. For isolated (nonperiodic) updrafts, the transform depends on the size of the domain over which it is calculated, which is inherently ambiguous. Third, it is unclear how well the functional forms of the single normal mode expansion capture horizontal gradients of buoyancy in real updrafts, and the consequences of errors in this representation are not well understood. These issues highlight challenges in applying single normal mode solutions to the problem and motivate the more general approach derived in section 3 for a better quantitative understanding.

Analytic solutions to (3) and (5) can also be obtained for more complicated forcings and boundary conditions using, for example, the method of Green's functions (Yau 1979). However, this approach still requires the use of analytically integrable forcing functions, and by construction it leads to rather complicated solutions compared to the single normal mode approach. Holton (1973) and Kuo and Raymond (1980) used a combined analytic–numerical approach, avoiding some of the aforementioned issues. They estimated the horizontal component of the Laplacian using the first term of a Fourier–Bessel expansion to reduce the equations to one dimension and then numerically integrated the vertical component. More recently, Pauluis and Garner (2006) described relationships between perturbation pressure, vertical velocity, and updraft diameter D and height H for a rising bubble using the Green's function of a second-order ordinary differential equation derived from a simplified, discretized version of the anelastic 3D equations of motion. Approximating the Green's function, they derived a simple pressure scaling of w as $(1 + D/H)^{-1/2}$, different from the scalings in Weisman et al. (1997) or those derived using single normal mode solutions of the p_B equation above having the form $(1 + D^2/H^2)^{-1/2}$ as well as the more general derivation in section 3. Specific reasons for these differences in the scalings are difficult to pinpoint, but the approaches are rather different. For example, unlike the single normal mode approach or the derivation in section 3, Pauluis and Garner (2006) did not assume a steady state: that is, they did not explicitly assume $\partial/\partial t = 0$ in the momentum equations. They also neglected all nonlinear advection terms analogous to linearizing the momentum equations in deriving the nonhydrostatic perturbation pressure, while some of these terms are retained in the derivation here.

An alternative analytic approach for approximating Δp and w is derived in the next section. Instead of using

single normal mode expansion or other techniques to solve (3)–(5), the momentum and mass continuity equations are first integrated separately with appropriate boundary conditions and then combined to estimate Δp (and w). This approach yields simplified solutions for Δp and w with a functional form similar to the single normal mode solutions (7)–(9) and from Weisman et al. (1997), although they differ quantitatively. Moreover, without having to approximate ρB using simple periodic wavelike functions, this approach leads to greater generality and avoids some of the conceptual problems mentioned above.

3. General theoretical derivation

In this section, general theoretical expressions for Δp and w are derived for 2D and axisymmetric quasi-3D convective updrafts. The basic idea is to specify a steady-state field of B, and then calculate the steady-state Δp and w in the updraft center associated with this. For simplicity, updrafts are treated as isolated regions of positive thermal buoyancy embedded in an environment with $B = 0$. Since relative differences in B between the updraft and environment are relevant for the dynamics, any value of B could be chosen for the environment so long as the updraft buoyancy is calculated relative to this. For 2D, updrafts are assumed to consist of a slab of positively buoyant air (relative to the environment). For 3D, updrafts are represented analogously by an axisymmetric cylinder of positively buoyant air. Entrainment is not explicitly included, which allows us to focus on the effects of perturbation pressure. However, the effects of entrainment on buoyancy are implicit in the specified distribution of buoyancy within the updraft.

a. Axisymmetric quasi-3D updraft model

For 3D flow, the derivation starts with the inviscid, anelastic momentum equation (Ogura and Phillips 1962), neglecting Coriolis acceleration, assuming a steady state, and separated into horizontal and vertical components and mass continuity in axisymmetric cylindrical coordinates:

$$\frac{\partial u}{\partial t} = -u\frac{\partial u}{\partial r} - w\frac{\partial u}{\partial z} - \frac{1}{\rho}\frac{\partial p}{\partial r} = 0, \tag{10}$$

$$\frac{\partial w}{\partial t} = -u\frac{\partial w}{\partial r} - w\frac{\partial w}{\partial z} - \frac{1}{\rho}\frac{\partial p}{\partial z} + B = 0, \quad \text{and} \tag{11}$$

$$\frac{\rho}{r}\frac{\partial (ru)}{\partial r} + \frac{\partial (\rho w)}{\partial z} = 0, \tag{12}$$

where r is distance along the radial direction, B is the perturbation buoyancy as defined in section 2, and all quantities except ρ are perturbations from a hydrostatic, motionless, horizontally homogeneous background state. By design, this framework neglects turbulence-scale fluctuations; that is, w and p are functions only of B (and ρ).

If the distribution of ρB is horizontally and vertically symmetric around the updraft center and the boundary conditions are symmetric, this implies horizontal symmetry and vertical antisymmetry of p, with the approximation that $p \sim p_B$. In this instance, $p < 0$ below the (LMB) where $\partial(\rho B)/\partial z > 0$; $p > 0$ above the LMB where $\partial(\rho B)/\partial z < 0$; and $p = 0$ at the LMB. This can be demonstrated using Fourier series expansion, indicating that $p \sim -\nabla^2 p$ for symmetric forcing functions. This general structure of p is reasonable even for cases in which ρB is not symmetric. It well approximates numerical solutions of the p_B field in Part II, except near the hydrostatic limit. It also reasonably approximates the total perturbation pressure in fully dynamical updraft simulations, such as that shown in Fig. 1. Thus, a structure of $p < 0$ below the LMB, $p > 0$ above the LMB, and $p = 0$ at the LMB is assumed for the derivation below. Since $p < 0$ below the LMB, this indicates a horizontal pressure gradient and net convergence across the updraft between the LFC and LMB, since perturbation pressure approaches 0 sufficiently far from the updraft and $u = 0$ at the updraft center.

The conceptual model also applies some assumptions about the horizontal distribution of perturbation pressure within the updraft. At the LFC, it is assumed that $\partial p/\partial r \sim 0$ across the updraft, consistent with the time-evolving, fully dynamical updraft simulation in Fig. 1 and the other simulations shown in Fig. 13 of Part II. This behavior in these simulations is approximately explained by the fact that $\partial p_B/\partial r \sim -\partial p_D/\partial r$ there, since p_B has a local minimum at the updraft center, while p_D has a local maximum (Figs. 1g,h). This overall flow pattern and approximate balance between horizontal gradients of p_B and p_D near the LFC is established rapidly in the simulations (within a few min) and is maintained as the updrafts grow in time. How does one reconcile $\partial p/\partial r \sim 0$ across the updraft near the LFC with the fact that there is horizontal inflow combined with $u = 0$ at the updraft center that would seem to imply $\partial p/\partial r < 0$ at this level? This is explained by the term $-w\partial u/\partial z$ in (10): given a sharp decrease in the magnitude of u below the LFC (Fig. 1a) and $w > 0$ implies a turning of this horizontal inflow upward within the updraft so that large horizontal gradients of p are not needed to decelerate the inflow at the LFC. The conceptual model makes no explicit assumptions about the structure of downdrafts and compensating subsidence surrounding the updraft, but it does assume that this downward motion has no direct impact on the perturbation pressure field of the updraft itself, as discussed below.

Multiplying the steady-state horizontal momentum equation [(10)] by ρ and integrating from $r = R$ to ∞ gives the following Bernoulli-like equation:

$$p_R = -\frac{\rho}{2}u_R^2 + \int_{r=R}^{\infty} \rho w \frac{\partial u}{\partial z} dr \approx -\frac{\rho}{2}u_R^2, \qquad (13)$$

similar to (6) in List and Lozowski (1970), where the boundary conditions are $p = 0$ and $u = 0$ in the far field at $r = \infty$. Here it assumed that the second term on the right-hand side is small compared to the first term. This is reasonable, given that the largest (magnitude) w tend to occur in conjunction with the smallest $\partial u/\partial z$, and vice versa, by mass continuity and the condition $u = 0$ in the far field. Moreover, this term vanishes at the LFC if $w \sim 0$ there. This is equivalent to neglecting the nonhydrostatic pressure outside of the updraft; that is, the environment is assumed to be in hydrostatic balance and act as an infinite mass reservoir (Pauluis and Garner 2006). Physically, this assumption means that the effects of downdrafts and compensating subsidence are not explicitly considered in calculating the perturbation pressure field of the updraft.

The perturbation pressure difference between the LMB and LFC Δp_1, which is needed for deriving w from the vertical momentum equation, is calculated following (13) by relating u_R between the LFC and LMB to w via mass continuity. An expression for the average u_R between any two levels can be found by noting that the difference in upward mass flux between the levels must be balanced by the vertical integral of the horizontal mass inflow between these levels, keeping in mind the variation of ρ with height. Thus,

$$\int_A \rho w = -\int_S \rho u_R, \qquad (14)$$

where the integral on the left-hand side is over the horizontal area of the updraft at z, and the integral on the right-hand side is over the lateral edge of the updraft between heights z_1 and z_2. Given the cylindrical geometry, (14) can be expressed in finite difference form as

$$\pi R^2(\rho_1 \overline{w}_1 - \rho_2 \overline{w}_2) = -2\pi R \overline{\rho u}_R (z_1 - z_2), \qquad (15)$$

where $\overline{w}$ is the average vertical velocity between $r = 0$ and $r = R$ at a given vertical level:

$$\overline{w} = \frac{\int_A w}{\pi R^2}, \qquad (16)$$

and $\overline{\rho}$ and $\overline{u}_R$ are the air density and radial velocity at $r = R$, respectively, averaged between z_1 and z_2.

The negative sign in (14) and (15) accounts for the fact that an upward increase in mass flux must be compensated by mass inflow (i.e., negative ρu_R). The integral in (16) depends upon how w varies horizontally across the updraft. Here, it is assumed that $\overline{w} = \alpha w_0$, where α is a parameter relating w at the updraft center w_0 to its horizontally averaged value across the updraft. The parameter α was employed in previous one-dimensional convective cloud models, as by Kuo and Raymond (1980), who assumed $\alpha = 0.5$. Hereinafter, the subscript "0" is neglected, and α is assumed to be constant with height. With this assumption, u_R averaged from the LFC to the LMB is given by

$$\overline{u}_R = -\frac{\alpha R}{2\overline{\rho}} \frac{(\rho_M w_M - \rho_F w_F)}{H_1} = -\frac{\alpha R}{2\overline{\rho}} \frac{\rho_M w_M}{H_1}, \qquad (17)$$

where $H_1 = z_M - z_F$, using the condition that $w_F = 0$ (subscripts F and M refer to values at the LFC and LMB, respectively). For simplicity, the Boussinesq approximation is applied hereafter so that variation of ρ with height is neglected. This results in generally small errors in w even for the deepest case tested in Part II, although there are larger relative errors in Δp. Specifically, numerical solutions in Part II show that differences in vertical velocity at the updraft center between anelastic and Boussinesq flows are small at the LNB and LMB (less than a few percent and less than 15%, respectively) and somewhat larger near the LFC (up to ~30%).

One cannot simply use $\overline{u}_R$ to calculate p_F following (13), because this is inconsistent with the boundary condition $p_M = 0$, which requires $u_R^2 = u_R = 0$ at the LMB. Thus, u_R must vary with height whenever $w > 0$: that is, in all conditions except at the hydrostatic limit. For simplicity, a linear profile of u_R with height is assumed between the LFC and LMB, which is reasonable based on fully dynamical updraft simulations (see Fig. 1a). Combining this assumption with (13), the condition that $u_R = 0$ at the LMB and the Boussinesq approximation gives

$$p_F = -\frac{\overline{\rho}\alpha^2 R^2}{2}\frac{w_M^2}{H_1^2}, \qquad (18)$$

where $\overline{\rho}$ is the average (Boussinesq) air density. The perturbation pressure difference between the LMB and LFC is then given by

$$\Delta p_1 = \frac{\overline{\rho}\alpha^2 R^2}{2}\frac{w_M^2}{H_1^2} \qquad (19)$$

using the boundary condition $p_M = 0$.

Next, w at the updraft center ($r = 0$) is derived by vertical integration of the steady-state vertical momentum equation [(11)]. Integration at $r = 0$ avoids complications associated with the term $-w\partial u/\partial z$, since $\partial u/\partial z = 0$ at $r = 0$. Results can then be expressed in terms of $\overline{w}$ via the parameter α. We therefore need to relate the Δp_1 given by (19), valid at $r = R$, to the perturbation pressure difference from the LMB to the LFC at $r = 0$, which is done by assuming p at the updraft center is equal to that at the lateral edge at the LFC, as discussed previously in this section ($p = 0$ at the center and edge of the updraft at the LMB).

Using (19) for the perturbation pressure difference from the LMB to the LFC at the updraft center, integrating (11) from the LFC to the LMB, and rearranging terms to solve for w_M gives

$$w_M = \sqrt{2\mathrm{CAPE}_1\left(1 + \frac{\alpha^2 R^2}{H_1^2}\right)^{-1}}, \tag{20}$$

where $\mathrm{CAPE}_1 = \int_{z_F}^{z_M} B\, dz$.

Combining (19) and (20) gives

$$\Delta p_1 = \overline{\rho}\mathrm{CAPE}_1\left(1 + \frac{H_1^2}{\alpha^2 R^2}\right)^{-1}. \tag{21}$$

If ρB is symmetric around the LMB, the solution of $\nabla^2 p_B = \partial(\rho B)/\partial z$ is antisymmetric around the LMB. This implies that the perturbation pressure difference from the LNB to the LMB Δp_2 can be approximated as

$$\Delta p_2 = \overline{\rho}\mathrm{CAPE}_2\left(1 + \frac{H_2^2}{\alpha^2 R^2}\right)^{-1}, \tag{22}$$

where $\mathrm{CAPE}_2 = \int_{z_M}^{z_N} B\, dz$ and $H_2 = z_N - z_M$, and it is assumed that $p \sim p_B$ and the flow is Boussinesq (subscript N refers to values at the LNB). Equation (22) can be combined with the steady-state vertical momentum equation integrated from the LMB to the LNB to give

$$w_N = \sqrt{2\mathrm{CAPE}_2\left(1 + \frac{\alpha^2 R^2}{H_2^2}\right)^{-1} + w_M^2}. \tag{23}$$

If the buoyancy profile is vertically symmetric from the LFC to LNB (meaning $H = 2H_1 = 2H_2$), then the perturbation pressure difference from the LNB to the LFC Δp is found by summing (21) and (22) to give

$$\Delta p = \overline{\rho}\mathrm{CAPE}\left(1 + \frac{H^2}{4\alpha^2 R^2}\right)^{-1}, \tag{24}$$

since $\mathrm{CAPE} = \mathrm{CAPE}_1 + \mathrm{CAPE}_2$. Combining (24) with the vertical momentum equation integrated from the LFC to the LNB gives

$$w_N = \sqrt{2\mathrm{CAPE}\left(1 + \frac{4\alpha^2 R^2}{H^2}\right)^{-1}}. \tag{25}$$

This indicates the same pressure scaling of w at the LMB and LNB when the buoyancy profile forcing is symmetric from the LFC to LNB, since $H = 2H_1$, which is expected. However, numerical solutions of the p_B field in Part II show that there is a vertical asymmetry even when the buoyancy profile from the LFC to the LNB is symmetric. This occurs for two reasons. The first is simply because a height-varying base state ρ is used for the numerical calculations. However, there is still a fundamental asymmetry in the numerical solutions even when ρ is constant: that is, when ρB from the LMB to LNB is a mirror image of that from the LFC to LMB. This is explained by the fact that updrafts are located nearer to the surface than the top of the atmosphere, meaning that the buoyancy forcing is not symmetric around the LMB even when the buoyancy profile is symmetric between the LFC and LNB. As a result, (23) tends to underestimate w_N because it does not take into account this vertical asymmetry.

This asymmetry suggests an additional length scale is needed even when ρB from the LFC to LNB is symmetric. Since updrafts are closer to the surface, this implies shorter wavelength Fourier modes of the buoyancy forcing are more dominant below the LMB with longer wavelength modes more dominant above. This leads to a relative decrease of $\partial p/\partial z$ in the upper part of the updraft and hence a "flattening" of the w profile; that is, $\partial w/\partial z$ becomes approximately constant with height when pressure effects are important [R/H of $O(1)$ and larger]. This flattening of the w profile is clearly seen from the numerical solutions detailed in Part II (see Fig. 12 therein).

To improve accuracy and account for this behavior in a simple way, analytic solutions are constructed based on the physical reasoning above and results of the numerical solutions in Part II. A simple approximation of the behavior of the numerical solutions is to estimate $\Delta p \sim 2\Delta p_1$ with $\partial w/\partial z$ taken as constant with height, meaning that $w_M/H_1 \sim w_N/H$ in (19), to give

$$\Delta p = \overline{\rho}\alpha^2 R^2 \frac{w_N^2}{H^2}. \tag{26}$$

Combining (26) with the vertical momentum equation integrated from the LFC to the LNB and using the Boussinesq approximation yields

$$w_N = \sqrt{2\text{CAPE}\left(1 + \frac{2\alpha^2 R^2}{H^2}\right)^{-1}}. \quad (27)$$

Combining (26) and (27) and rearranging terms gives

$$\Delta p = \overline{\rho}\text{CAPE}\left(1 + \frac{H^2}{2\alpha^2 R^2}\right)^{-1}. \quad (28)$$

With this approximation, the pressure reduction of w_M relative to the thermodynamic maximum is up to a factor of $\sqrt{2}$ larger than the relative reduction of w_N for a vertically symmetric buoyancy profile with $H_1 = H/2$. This approach well captures vertical asymmetries in the numerically calculated p_B field, which is detailed in Part II (section 3d).

b. Derivation in 2D Cartesian coordinates

If the anelastic mass continuity equation in axisymmetric cylindrical coordinates given by (12) is replaced with that for 2D Cartesian coordinates,

$$\frac{\partial(\rho u)}{\partial x} + \frac{\partial(\rho w)}{\partial z} = 0, \quad (29)$$

then (15) is expressed as

$$2R(\rho_1 \overline{w}_1 - \rho_2 \overline{w}_2) = -2\overline{\rho}\overline{u}_R(z_1 - z_2). \quad (30)$$

Solving for u_R as described above for 3D, using this expression for u_R in the perturbation pressure equation, and applying the same procedure as described above, expressions for w_M and w_N for 2D updrafts analogous to (20) and (27) are derived:

$$w_M = \sqrt{2\text{CAPE}_1\left(1 + \frac{4\alpha^2 R^2}{H_1^2}\right)^{-1}} \quad \text{and} \quad (31)$$

$$w_N = \sqrt{2\text{CAPE}\left(1 + \frac{8\alpha^2 R^2}{H^2}\right)^{-1}}. \quad (32)$$

We can similarly calculate the perturbation pressure difference between the LNB and LFC:

$$\Delta p = \overline{\rho}\text{CAPE}\left(1 + \frac{H^2}{8\alpha^2 R^2}\right)^{-1}. \quad (33)$$

Comparing (28) and (33) shows that, in 2D flow, there is an increase in the pressure difference relative to 3D that is a direct consequence of differences in the continuity equation between 2D and 3D. The 2D and 3D expressions for Δp both approach the hydrostatic perturbation pressure difference at the hydrostatic limit as $R/H \to \infty$, consistent with the idea that hydrostatic balance should not depend on dimensionality.

4. Discussion

The theoretical expressions derived in the previous section indicate a dependence of Δp and w on the square of a nondimensional length $L_C \equiv \alpha R/H$. Thus, perturbation pressure effects depend on the ratio R/H, consistent with the physical arguments and scaling from Weisman et al. (1997) discussed in the introduction and the single normal mode solutions in section 2. There is also a dependence on α, which reflects the impact of the shape of the vertical velocity distribution across the updraft on the perturbation pressure. The case of $\alpha = 0$ is analogous to $R = 0$.

Limiting cases are discussed next. For $R/H \to \infty$ in (20), (27), (31), and (32), corresponding to the hydrostatic limit, then $w \to 0$ as expected for a buoyancy perturbation of infinite width. On the other hand, for $L_C \ll 1$, perturbation pressure effects are negligible, and (27) and (32) reduce to the parcel equation $w = \sqrt{2\text{CAPE}}$, representing the maximum w in the absence of perturbation pressure effects. For the hydrostatic regime when $L_C \gg 1$, (27) is reduced to

$$w_N \approx \frac{H}{\alpha R}\sqrt{\text{CAPE}} \quad (34)$$

for 3D updrafts. Analogously, the hydrostatic regime for 2D gives

$$w_N \approx \frac{H}{2\alpha R}\sqrt{\text{CAPE}}. \quad (35)$$

These expressions suggest that 2D updrafts are a factor of 2 weaker than 3D for hydrostatic flow, all else being equal, with smaller relative differences as L_C decreases in the nonhydrostatic regime. They also show that nonhydrostatic effects become important (>10% difference between the hydrostatic and nonhydrostatic w_N) when the nondimensional length $L_C \equiv \alpha R/H$ is less than 1.54 for 3D and 0.77 for 2D.

It is clear from (34) and (35) that the hydrostatic system will overestimate w for L_C of $O(1)$ or less; as $R/H \to 0$, then $w \to \infty$. Overprediction of w for relatively small R in the hydrostatic system is well known and has been discussed in previous papers (e.g., Orlanski 1981; Weisman et al. 1997). Physically, this is a consequence of the direct coupling of the inertial terms in the u momentum equation with horizontal gradients of (hydrostatic) perturbation pressure in the hydrostatic system; as $R/H \to 0$, then $\partial p/\partial r \to \infty$, implying $-\partial u/\partial r \to \infty$ and hence $\partial w/\partial z \to \infty$ by continuity. For the

nonhydrostatic system, the nonhydrostatic pressure gradient force increasingly balances the hydrostatic perturbation pressure gradient force as $R/H \to 0$; at $R/H = 0$, $\partial p_{\rm NH}/\partial z = -\partial p_H/\partial z$. In other words, at $R/H = 0$ the nonhydrostatic and hydrostatic perturbation pressure gradients are in exact balance, the total perturbation pressure gradient is zero, and maximum conversion of potential to kinetic energy occurs. Thus, the "1" in the denominator of (20), (27), (31), and (32) represents the influence of the nonhydrostatic pressure and is a direct consequence of the inertial term $(1/2)[\partial(w^2)/\partial z]$ in the vertical momentum equation that is neglected in the hydrostatic system. Similar differences between hydrostatic and nonhydrostatic vertical motion for 2D were discussed by Weisman et al. (1997) based on the scalings given by (1) in the introduction, although they did not describe these effects in terms of hydrostatic and nonhydrostatic perturbation pressures.

It is useful to point out that the expressions for Δp given by (28) and (33) include both the nonhydrostatic and hydrostatic perturbation pressures. This may not be obvious since Δp is derived from the u momentum equation, which includes the inertial and advective terms for u but does not include B. However, linkage of the u momentum equation to p_H occurs implicitly via mass continuity and the vertical momentum equation, providing a bridge between $(1/r)[\partial(ru)/\partial r]$ and $\partial w/\partial z$ and, hence, the buoyancy and hydrostatic perturbation pressure. In contrast, linkage of the u momentum equation with p_H is explicit in the hydrostatic system, since this system directly relates horizontal gradients of p_H to the inertial and advective terms in the u momentum equation, while neglecting the vertical momentum equation and nonhydrostatic pressure. The fact that the expressions for Δp derived here include the hydrostatic perturbation pressure can be easily demonstrated by taking $R/H \to \infty$ in (28) and (33), which recovers the Boussinesq vertically integrated hydrostatic perturbation pressure difference from the LNB to the LFC equal to $\overline{\rho}$CAPE. The nonhydrostatic perturbation pressure difference between the LNB and LFC is simply given by $\Delta p - \overline{\rho}$CAPE and approaches 0 at the hydrostatic limit.

These expressions for Δp and w are similar to those from Weisman et al. (1997) and derived using the single Fourier/Fourier–Bessel normal mode approach given by (7)–(9), with a pressure scaling of w having the form $(1 + R^2/H^2)^{-1/2}$. However, there are conceptual and quantitative differences. The general approach herein (section 3) first integrates the momentum and mass continuity equations separately, providing important integral constraints on the solutions. Thus, Δp and w are expressed in terms of the vertically integrated buoyancy (CAPE), and this provides physically consistent solutions at the limits $R/H \to 0$ and $R/H \to \infty$ that are bounded by these constraints. Single normal mode solutions do not follow these constraints unless the vertical integral of the single mode representation of ρB over the updraft is exact. Moreover, the single normal mode approach by its construct cannot capture vertical asymmetries in the pressure scaling of w between the LFC and LMB and between the LMB and LNB, which are evident in the numerical solutions and important in explaining vertical profiles of w, as shown in Part II. The approach in section 3 is also more general because relationships between quantities averaged across the updraft and at its center are encapsulated by the parameter α but are implicit in the normal mode approach based on the functional forms of the series expansions. For isolated (nonperiodic) updrafts, a Fourier or Fourier–Bessel transform of the buoyancy forcing is also dependent upon the size of the domain over which the transform is calculated, which is inherently ambiguous.

Finally, it is emphasized that the derivation is non-Archimedean, in the sense that it does not depend on the assumed background thermodynamic state (and hence on the mass of the environment displaced by the updraft), even though the buoyancy itself is Archimedean. If the background thermodynamic state has nonzero B (and hence, by definition, nonzero p_H), then the background state and hydrostatic pressure can simply be redefined so $B = 0$ and $p_H = 0$. This is consistent with the expressions for Δp and w above when $R/H \to \infty$; that is, when the region of perturbed buoyancy is infinitely wide, the total pressure perturbation is equal to p_H and $w = 0$.

5. Summary and conclusions

This study investigated the role of perturbation pressure on the vertical velocity w of buoyant updraft cores. In the current paper, Part I, simple theoretical expressions relating w and the perturbation pressure difference from the level of neutral buoyancy (LNB) to the level of free convection (LFC) Δp to updraft radius R, height H, and CAPE for 2D and axisymmetric quasi-3D flows were derived based on approximate analytic solutions to the governing momentum and mass continuity equations. A key assumption in the derivation was that the flow is steady state, linking this work to the steady-state plume conceptual model. However, the perturbation pressure is diagnostic from the buoyancy and wind fields at any instance in time (or nearly diagnostic in the case of compressible flow), as described in Part II, implying that the steady-state assumption is by itself unimportant in the theoretical derivation of perturbation pressure as long as the buoyancy field is known. Thus, the

theoretical expressions for perturbation pressure match well with fully dynamical, time-evolving updraft simulations, as detailed in Part II, especially early in the simulations before entrainment begins to dominate. The steady-state assumption is more important for w, since $\partial w/\partial t$ appears directly in the vertical momentum equation.

The other main assumptions in deriving the theoretical expressions were as follows: 1) neglect of the impact of downdrafts on updraft dynamics; 2) $p = 0$ at the level of maximum buoyancy (LMB); 3) the u wind profile is linear with height from the LFC to the LMB; 4) w at the updraft center is proportional to the w averaged across the updraft by the parameter α, which is constant with height; 5) the environment is unsheared; and 6) variation of air density ρ is neglected except where coupled to the buoyancy following the Boussinesq approximation. Despite these idealizations, the theoretical expressions show a close correspondence with numerical calculations of the anelastic buoyant perturbation pressure Poisson equation over a wide range of conditions, as well as fully dynamical updraft simulations, as detailed in Part II.

The theoretical expressions show a scaling of w by factors of $(1 + 8L_C^2)^{-1/2}$ and $(1 + 2L_C^2)^{-1/2}$ at the LNB for 2D and 3D, respectively, compared to the theoretical maximum $\sqrt{2\text{CAPE}}$, where $L_C \equiv \alpha R/H$ is a nondimensional length. The nondimensional aspect of this scaling suggests that pressure effects on w are potentially important not only in deep updrafts but also shallow convection, depending upon the ratio of updraft width to height. The scaling of w from perturbation pressure is somewhat different lower in the updraft than at the LNB, even when the buoyancy forcing is symmetric from the LFC to the LNB. This reflects a vertical asymmetry caused by updrafts that are located nearer to the surface than the top of the atmosphere (see section 3d in Part II). While functional forms for the scalings of Δp and w with R and H are similar, this approach is more general and avoids some of the challenges in applying single normal mode solutions using Fourier or Fourier–Bessel expansion.

Fundamental differences in mass continuity led to differences in the theoretical scalings of Δp and w between 2D and 3D updrafts. This provides a concise physical explanation for weaker updrafts in 2D than 3D reported in many previous modeling studies. Relative differences in w between 2D and 3D are up to a factor of 2 for $L_C \gg 1$, with differences vanishing for $L_C \to 0$. The theoretical solutions also indicate that nonhydrostatic effects become significant (greater than 10% difference between hydrostatic and nonhydrostatic w_N) for L_c less than 1.54 for 3D and less than 0.77 for 2D. Differences in the theoretical hydrostatic and nonhydrostatic scalings arise directly from the $w\partial w/\partial z$ term in the vertical momentum equation, which is neglected in hydrostatic flow. This provides a quantitative description of the hydrostatic–nonhydrostatic transition based on the nondimensional length L_c and suggests interesting differences in this transition for 2D versus 3D flow.

The role of environmental wind shear was neglected. These results are therefore most applicable to cumulus convection in weakly sheared environments. Nonetheless, it is expected that the proposed expressions can approximately describe the scaling of w with R and H in sheared environments, since buoyant perturbation pressure still plays a key role in these conditions.

Here, α was assumed to be an externally specified parameter constant with height. Future work should clarify values of α and their vertical variation, including the linkage with entrainment, by extending the idealized model as well as analysis of fully dynamical simulations. Additional work is needed to understand the role of other key idealizations in the derivation, especially neglecting the role of downdrafts on updraft dynamics. Solutions with compensating subsidence occurring by solitary gravity waves propagating away from isolated updrafts (treated as regions of diabatic heating) are readily obtained for hydrostatic flow (Bretherton and Smolarkiewicz 1989). However, in addition to nonhydrostatic effects, a challenge is that downdraft dynamics are strongly coupled to complicated microphysical processes, leading to generation of negatively buoyant moist downdrafts (relative to the environment), for which a general theory is lacking. Different geometries in 2D and 3D suggest differences in compensating subsidence and downdrafts between 2D and 3D flow, as also indicated by fully dynamical simulations (e.g., Phillips and Donner 2006). Future work will investigate these aspects.

Here, updrafts were represented as buoyant plumes (as is typically assumed in convection parameterizations). However, real atmospheric moist convection, especially shallow convection, often has characteristics more resembling rising thermals than entraining/detraining plumes [see discussion in Sherwood et al. (2013)]. This is especially evident from modeling studies at high resolution [Δx of $O(100)$ m] , whereas at lower resolution moist convection seems to have a more plumelike appearance [cf., Fig. 3 in Bryan and Morrison (2012)]. Comparing and contrasting perturbation pressure effects for thermal- versus plume-based representations of moist convection is beyond the scope of this study but is currently being investigated.

Acknowledgments. This work was partially supported by U.S. DOE ASR DE-SC0008648, NASA NNX14AO85G, and the NSF Science and Technology Center for Multiscale Modeling of Atmospheric Processes (CMMAP), managed by Colorado State University under Cooperative Agreement ATM-0425247. The author thanks G. Bryan, R. Rotunno, W. Grabowski, and Z. Lebo for discussions, R. Rotunno and W. Grabowski for comments on an earlier version of the manuscript, G. Bryan for developing and maintaining CM1, and P. Markowski for code used to separate the various contributions of perturbation pressure in CM1.

REFERENCES

Árnason, G., R. S. Greenfield, and E. A. Newburg, 1968: A numerical experiment in dry and moist convection including the rain stage. *J. Atmos. Sci.*, **25**, 404–415, doi:10.1175/1520-0469(1968)025<0404:ANEIDA>2.0.CO;2.

Barnes, S. L., 1970: Some aspects of a severe, right-moving thunderstorm deduced from mesonetwork rawinsonde observations. *J. Atmos. Sci.*, **27**, 634–648, doi:10.1175/1520-0469(1970)027<0634:SAOASR>2.0.CO;2.

Bluestein, H. B., 2013: *Severe Convective Storms and Tornados.* Springer Berlin Heidelberg, 456 pp.

Bretherton, C. S., and P. K. Smolarkiewicz, 1989: Gravity waves, compensating subsidence and detrainment around cumulus clouds. *J. Atmos. Sci.*, **46**, 740–759, doi:10.1175/1520-0469(1989)046<0740:GWCSAD>2.0.CO;2.

Bryan, G. H., and J. M. Fritsch, 2002: A benchmark simulation for moist nonhydrostatic numerical models. *Mon. Wea. Rev.*, **130**, 2917–2928, doi:10.1175/1520-0493(2002)130<2917:ABSFMN>2.0.CO;2.

——, and H. Morrison, 2012: Sensitivity of a simulated squall line to horizontal resolution and parameterization of microphysics. *Mon. Wea. Rev.*, **140**, 202–225, doi:10.1175/MWR-D-11-00046.1.

Byers, H. R., and R. R. Braham, 1949: *The Thunderstorm.* U. S. Government Printing Office, 287 pp.

Davies-Jones, R., 2003: An expression for effective buoyancy in surroundings with horizontal density gradients. *J. Atmos. Sci.*, **60**, 2922–2925, doi:10.1175/1520-0469(2003)060<2922:AEFEBI>2.0.CO;2.

Doswell, C. A., III, and P. M. Markowski, 2004: Is buoyancy a relative quantity? *Mon. Wea. Rev.*, **132**, 853–863, doi:10.1175/1520-0493(2004)132<0853:IBARQ>2.0.CO;2.

Fujita, T., 1955: Results of detailed synoptic studies of squall lines. *Tellus*, **7A**, 405–436, doi:10.1111/j.2153-3490.1955.tb01181.x.

Holton, J. R., 1973: A one-dimensional cumulus model including pressure perturbations. *Mon. Wea. Rev.*, **101**, 201–205, doi:10.1175/1520-0493(1973)101<0201:AOCMIP>2.3.CO;2.

Klemp, J. B., 1987: Dynamics of tornadic thunderstorms. *Annu. Rev. Fluid Mech.*, **19**, 369–402, doi:10.1146/annurev.fl.19.010187.002101.

Kuo, H. L., and W. H. Raymond, 1980: A quasi-one-dimensional cumulus cloud model and parameterization of cumulus heating and mixing effects. *Mon. Wea. Rev.*, **108**, 991–1009, doi:10.1175/1520-0493(1980)108<0991:AQODCC>2.0.CO;2.

Lipps, F. B., and R. S. Hemler, 1986: Numerical simulation of deep tropical convection associated with large-scale convergence. *J. Atmos. Sci.*, **43**, 1796–1816, doi:10.1175/1520-0469(1986)043<1796:NSODTC>2.0.CO;2.

List, R., and E. P. Lozowski, 1970: Pressure perturbations and buoyancy in convective clouds. *J. Atmos. Sci.*, **27**, 168–170, doi:10.1175/1520-0469(1970)027<0168:PPABIC>2.0.CO;2.

Markowski, P., and Y. Richardson, 2010: *Mesoscale Meteorology in Midlatitudes.* Wiley-Blackwell, 430 pp.

Morrison, H., 2015: Impacts of updraft size and dimensionality on the perturbation pressure and vertical velocity in cumulus convection. Part II: Comparison of theoretical and numerical solutions and fully dynamical simulations. *J. Atmos. Sci.*, **73**, 1455–1480, doi:10.1175/JAS-D-15-0041.1.

Murray, F. W., 1970: Numerical models of a tropical cumulus cloud with bilateral and axial symmetry. *Mon. Wea. Rev.*, **98**, 14–28, doi:10.1175/1520-0493(1970)098<0014:NMOATC>2.3.CO;2.

Ogura, Y., and N. A. Phillips, 1962: Scale analysis of deep and shallow convection in the atmosphere. *J. Atmos. Sci.*, **19**, 173–179, doi:10.1175/1520-0469(1962)019<0173:SAODAS>2.0.CO;2.

Orlanski, I., 1981: The quasi-hydrostatic approximation. *J. Atmos. Sci.*, **38**, 572–582, doi:10.1175/1520-0469(1981)038<0572:TQHA>2.0.CO;2.

Parker, M. D., 2010: Relationship between system slope and updraft intensity in squall lines. *Mon. Wea. Rev.*, **138**, 3572–3578, doi:10.1175/2010MWR3441.1.

Pauluis, O., and S. Garner, 2006: Sensitivity of radiative–convective equilibrium simulations to horizontal resolution. *J. Atmos. Sci.*, **63**, 1910–1923, doi:10.1175/JAS3705.1.

Phillips, V. T. J., and L. J. Donner, 2006: Cloud microphysics, radiation and vertical velocities in two- and three-dimensional simulations of deep convection. *Quart. J. Roy. Meteor. Soc.*, **132**, 3011–3033, doi:10.1256/qj.05.171.

Redelsperger, J. L., and Coauthors, 2000: A GCSS model intercomparison for a tropical squall line observed during TOGA-COARE. I: Cloud-resolving models. *Quart. J. Roy. Meteor. Soc.*, **126**, 823–863, doi:10.1002/qj.49712656404.

Rotunno, R., and J. B. Klemp, 1982: The influence of the shear-induced pressure gradient on thunderstorm motion. *Mon. Wea. Rev.*, **110**, 136–151, doi:10.1175/1520-0493(1982)110<0136:TIOTSI>2.0.CO;2.

Schlesinger, R. E., 1973: A numerical model of deep moist convection: Part I. Comparative experiments for variable ambient moisture and wind shear. *J. Atmos. Sci.*, **30**, 835–856, doi:10.1175/1520-0469(1973)030<0835:ANMODM>2.0.CO;2.

——, 1984: Effects of the pressure perturbation field in numerical models of unidirectionally sheared thunderstorm convection: Two versus three dimensions. *J. Atmos. Sci.*, **41**, 1571–1587, doi:10.1175/1520-0469(1984)041<1571:EOTPPF>2.0.CO;2.

Sherwood, S. C., D. Hernandaz-Deckers, M. Colin, and F. Robinson, 2013: Slippery thermals and cumulus entrainment paradox. *J. Atmos. Sci.*, **70**, 2426–2442, doi:10.1175/JAS-D-12-0220.1.

Soong, S.-T., and Y. Ogura, 1973: A comparison between axisymmetric and slab-symmetric cumulus cloud models. *J. Atmos. Sci.*, **30**, 879–893, doi:10.1175/1520-0469(1973)030<0879:ACBAAS>2.0.CO;2.

Tao, W.-K., J. Simpson, and S.-T. Soong, 1987: Statistical properties of a cloud ensemble: A numerical study. *J. Atmos. Sci.*, **44**, 3175–3187, doi:10.1175/1520-0469(1987)044<3175:SPOACE>2.0.CO;2.

Trapp, R. J., 2013: *Mesoscale-Convective Processes in the Atmosphere.* Cambridge University Press, 377 pp.

Weisman, M. L., and J. B. Klemp, 1982: The dependence of numerically simulated convective storms on vertical wind shear and buoyancy. *Mon. Wea. Rev.*, **110**, 504–520, doi:10.1175/1520-0493(1982)110<0504:TDONSC>2.0.CO;2.

——, W. C. Skamarock, and J. B. Klemp, 1997: The resolution dependence of explicitly modeled convective systems. *Mon. Wea. Rev.*, **125**, 527–548, doi:10.1175/1520-0493(1997)125<0527:TRDOEM>2.0.CO;2.

Wilhelmson, R., 1974: The life cycle of a thunderstorm in three dimensions. *J. Atmos. Sci.*, **31**, 1629–1651, doi:10.1175/1520-0469(1974)031<1629:TLCOAT>2.0.CO;2.

Yau, M. K., 1979: Perturbation pressure and cumulus convection. *J. Atmos. Sci.*, **36**, 690–694, doi:10.1175/1520-0469(1979)036<0690:PPACC>2.0.CO;2.

Zeng, X., W.-K. Tao, S. Lang, A. Y. Hou, M. Zhang, and J. Simpson, 2008: On the sensitivity of atmospheric ensembles to cloud microphysics in long-term cloud-resolving model simulations. *J. Meteor. Soc. Japan*, **86A**, 45–65, doi:10.2151/jmsj.86A.45.